



Science Arts & Métiers (SAM)

is an open access repository that collects the work of Arts et Métiers Institute of Technology researchers and makes it freely available over the web where possible.

This is an author-deposited version published in: <https://sam.ensam.eu>
Handle ID: <http://hdl.handle.net/10985/23583>

To cite this version :

Jianchang ZHU, Mohamed BEN BETTAIEB, Farid ABED-MERAIM, M.S. HUANG, Z.H. LI -
Coupled effects of crystallographic orientation and void shape on ductile failure initiation using a CPFE framework - Engineering Fracture Mechanics - Vol. 280, p.109121 - 2023

Any correspondence concerning this service should be sent to the repository

Administrator : scienceouverte@ensam.eu



Coupled effects of crystallographic orientation and void shape on ductile failure initiation using a CPFE framework

J.C. Zhu^a, M. Ben Bettaieb^b, F. Abed-Meraim^b, M.S. Huang^{a,c,*}, Z.H. Li^{a,c}

^a Department of Mechanics, School of Aerospace Engineering, Huazhong University of Science and Technology, Wuhan 430074, PR China

^b Université de Lorraine, CNRS, Arts et Métiers Institute of Technology, LEM3, F-57070 Metz, France

^c Hubei Key Laboratory of Engineering Structural Analysis and Safety Assessment, Wuhan 430074, PR China

A B S T R A C T

Ductile failure reveals to be an anisotropic phenomenon, for which the proper mechanism has not been clearly addressed yet in the literature. In this paper, the effects of some key anisotropy factors on ductile failure initiation, detected by void coalescence and plastic strain localization, are investigated using unit-cell computations based on crystal plasticity finite element method. The studied anisotropic effects are induced by the combination of initial crystallographic orientations and void shapes. Therefore, single crystals with three different initial orientations and polycrystalline aggregates with three different initial crystallographic textures are respectively considered. A single void with either spherical, prolate or oblate shape is assumed to be preexisting at the center of each unit cell. By contrast to previous analyses in the literature, plastic strain localization is predicted in the present study on the basis of bifurcation theory. To cover a wide range of stress states, the simulations are performed under two macroscopic loading configurations: proportional triaxial stressing, characterized by constant stress triaxiality and Lode parameter, and proportional in-plane straining, specified by constant strain-path ratio. The obtained results show that the combined anisotropic effects play an important role in the occurrence of void coalescence and plastic strain localization, as well as in the competition between them.

1. Introduction

Over the past few decades, ductile failure of polycrystalline materials has been the object of great interest to both metal forming industry and community of plasticity mechanics. The initiation of ductile failure is often marked by two phenomena [1]: void coalescence and plastic strain localization. The former is caused by the evolution of ductile damage (which usually manifests itself in the form of microvoids), while the latter is a plastic instability phenomenon characterized by the occurrence of localized necking. These two phenomena are generally separate and their competition leads to final failure [1,2]. The progress in the fundamental understanding of the mechanisms related to these two phenomena has enabled safe design for engineering materials and structures. In this field, one can quote the recent advances in material characterization techniques, such as in-situ X-ray computed tomography, which allow direct visualization of damage evolution until failure initiation [3,4]. Despite the modern improvement in experimental techniques, it is still time-consuming, tedious and expensive to conduct experimental parametric studies of some relevant microstructural

* Corresponding author at: Department of Mechanics, School of Aerospace Engineering, Huazhong University of Science and Technology, Wuhan 430074, PR China.

E-mail address: mshuang@hust.edu.cn (M.S. Huang).

effects on failure initiation. Therefore, to achieve profound knowledge of these effects, theoretical and numerical tools are still indispensable.

Unit-Cell (UC) computation within finite element framework revealed to be an effective numerical tool for a comprehensive analysis of ductile failure [5]. In the context of UC computation, the mechanical response of the bulk material is assumed to be reproduced by a single UC subjected to relevant boundary conditions. This UC is viewed as representative of a heterogeneous medium made of two main phases: a void surrounded by a dense metal matrix (which may be itself made of several metallurgical phases). The mechanical behavior of the dense metal matrix can be described by either phenomenological constitutive models (see, e.g., Refs. [2,6–10]) or crystal plasticity frameworks (see, e.g., Refs. [11–18]). Using phenomenological constitutive models, researchers have developed various criteria to predict the onset of plastic strain localization and void coalescence within the UC. For instance, Wong and Guo [8] have established an energy-based criterion to predict the onset of void coalescence and final failure. Based on this criterion, Guo and Wong [7] have proposed an approach involving a macroscopic reaction force of UC to conduct strain localization analysis in voided metal sheets. Luo and Gao [19] have presented a sandwiched UC model consisting of three void-containing material units to analyze the occurrence of the two above-mentioned phenomena. Recently, Zhu et al. [2] have adopted the periodic homogenization scheme to investigate the competition between void coalescence and plastic strain localization, whose occurrences are respectively predicted by the energy-based criterion of Wong and Guo [8] and the Rice bifurcation analysis [20]. Although these investigations have provided reliable computational models and enriched our understanding of ductile failure by void coalescence and plastic strain localization, they cannot account for some relevant microstructural effects, such as crystallographic orientation and matrix heterogeneity, due to some conceptual limitations of phenomenological models. By contrast, crystal plasticity (CP) models naturally consider these effects and hence have been adopted in UC computations to study ductile failure initiation. UC strategies based on CP models have mainly been focused on void growth and coalescence in single crystals [11–16,21]. It has been demonstrated that the void behavior is strongly dependent on several factors, such as the stress state [11,12,15], the crystal orientation [15,16], the initial void volume fraction [13], among others. For polycrystals, in addition to the effects observed in single crystals, some features induced by the polycrystalline characteristics, such as matrix heterogeneity, orientation distribution, and grain size, also play significant roles in ductile failure initiation. These features complicate the mechanism of ductile failure in polycrystalline aggregates. Moreover, few number of investigations on polycrystalline aggregates have been devoted to the void growth stage [17,18,22]. It has been revealed that the matrix heterogeneity tends to retard the void growth, as compared to the case of homogeneous matrix [17]. In fact, the void growth rate in polycrystals is slower than in single crystals with the same void-containing grain orientation [18]. Furthermore, the void behavior and ductility of materials are grain-size dependent; for instance, the deformation heterogeneity and scatter of void growth tend to increase with grain size [22]. Overall, ductile failure initiation triggered by void coalescence and plastic strain localization in polycrystalline aggregates has not been sufficiently investigated yet.

In order to gain more insight into ductile failure initiation, both voided single crystals and polycrystalline aggregates are considered in the present study. The single crystal behavior follows a rate-independent formulation, where the plastic flow is governed by the Schmid law. The polycrystalline aggregates are generated by the Voronoi tessellation technique to accurately describe the grain morphology. The overall mechanical behavior of UC is determined by the crystal plasticity finite element (CPFE) based periodic homogenization framework. Void coalescence is predicted by the strain-based criterion developed in [23]. On the other hand, plastic strain localization is predicted by the Rice bifurcation criterion [20]. The single crystal results are presented for comparison purposes with polycrystalline cases. Both the single crystals and polycrystalline aggregates in the present work exhibit strong anisotropic behavior due to the individual or combined effects of initial void shape and crystallographic orientation, and their evolutions during plastic deformation. Plastic anisotropy induced by crystallographic orientation [9,24,25] or by void shape [26] has been demonstrated to significantly affect the void growth, but those investigations have been conducted using phenomenological models for the description of the mechanical behavior of the dense matrix. In the present paper, the combined anisotropic effects on plastic strain localization and void coalescence using the CPFE-based strategy are specifically analyzed.

The remainder of this paper is organized as follows: Section 2 gives some details on the computational modeling, including crystal plasticity constitutive equations, unit-cell formulation, mechanical loadings, boundary conditions, and the criteria adopted to predict plastic strain localization and void coalescence; Section 3 presents the results and corresponding discussion; Section 4 ends the paper with some conclusions.

2. Computational modeling

2.1. Crystal plasticity constitutive equations

In the present study, a rate-independent crystal plasticity formulation is adopted. The main constitutive equations at the single crystal scale are outlined in this section (further details about this formulation are provided in [27,28]). As a starting point, the velocity gradient \mathbf{g} is additively split into its symmetric and skew-symmetric parts, denoted as \mathbf{d} and \mathbf{w} , respectively. In addition, the strain rate tensor \mathbf{d} and the spin rate tensor \mathbf{w} are decomposed into their elastic and plastic parts, respectively:

$$\mathbf{d} = \frac{1}{2}(\mathbf{g} + \mathbf{g}^T) ; \quad \mathbf{w} = \frac{1}{2}(\mathbf{g} - \mathbf{g}^T) ; \quad \mathbf{d} = \mathbf{d}_e + \mathbf{d}_p ; \quad \mathbf{w} = \mathbf{w}_e + \mathbf{w}_p \quad (1)$$

Within the present crystal plasticity framework, the slip on crystallographic planes is considered as the only source of plastic flow, which writes:

Table 1

Elasticity and hardening parameters used in the simulations.

E (GPa)	ν	τ_0 (MPa)	h_0 (MPa/s)	n
65	0.3	40	390	0.184

$$\mathbf{d}_p = \sum_{\alpha=1}^{N_s} \dot{\gamma}^\alpha \mathbf{R}^\alpha ; \quad \mathbf{w}_p = \sum_{\alpha=1}^{N_s} \dot{\gamma}^\alpha \mathbf{S}^\alpha \quad (2)$$

where:

- $\dot{\gamma}^\alpha$ refers to the slip rate on the α -th slip system.
- N_s is the total number of slip systems (equal to twelve, as FCC single crystals with $\{111\} \langle 110 \rangle$ slip systems are considered in the present investigation).
- \mathbf{R}^α (resp. \mathbf{S}^α) is the symmetric part (resp. skew-symmetric part) of the Schmid tensor \mathbf{M}^α , which is equal to the tensor product of the slip direction vector $\bar{\mathbf{m}}^\alpha$ and the vector normal to the slip plane $\bar{\mathbf{n}}^\alpha$:

$$\forall \alpha = 1, \dots, N_s : \mathbf{M}^\alpha = \bar{\mathbf{m}}^\alpha \otimes \bar{\mathbf{n}}^\alpha \quad (3)$$

The elastic behavior of the single crystal is assumed to be isotropic¹, and described by a hypoelastic law, which relates the lattice co-rotational rate $\dot{\boldsymbol{\sigma}}^\nabla$ of the Cauchy stress tensor $\boldsymbol{\sigma}$ to the elastic strain rate \mathbf{d}_e , using the fourth-order elasticity tensor \mathbf{C}_e :

$$\dot{\boldsymbol{\sigma}}^\nabla = \dot{\boldsymbol{\sigma}} - \mathbf{w}_e \cdot \boldsymbol{\sigma} + \boldsymbol{\sigma} \cdot \mathbf{w}_e = \mathbf{C}_e : \mathbf{d}_e \quad (4)$$

For rate-independent behavior, the plastic flow rule is governed by the Schmid law, which states that a slip system is activated only if the absolute value of the resolved shear stress τ^α reaches a critical value τ_c^α :

$$\forall \alpha = 1, \dots, N_s : |\tau^\alpha| \leq \tau_c^\alpha ; \quad (|\tau^\alpha| - \tau_c^\alpha) \dot{\gamma}^\alpha = 0 \quad (5)$$

where τ^α is defined in terms of $\boldsymbol{\sigma}$ and \mathbf{R}^α as:

$$\forall \alpha = 1, \dots, N_s : \tau^\alpha = \boldsymbol{\sigma} : \mathbf{R}^\alpha \quad (6)$$

The critical shear stress τ_c^α evolves with the slip accumulation on the crystallographic slip systems as follows:

$$\forall \alpha = 1, \dots, N_s : \dot{\tau}_c^\alpha = \sum_{\beta=1}^{N_s} H^{\alpha\beta} |\dot{\gamma}^\beta| \quad (7)$$

where $H^{\alpha\beta}$ is the $\alpha\beta$ component of the hardening matrix \mathbf{H} , which is dependent on the accumulated slip of different slip systems. Following the formulation adopted in [29], isotropic hardening is assumed and the components of hardening matrix $H^{\alpha\beta}$ are given by the following expression:

$$\forall \alpha, \beta = 1, \dots, N_s : H^{\alpha\beta} = h_0 \left(1 + \frac{h_0 \Gamma}{\tau_0 n} \right)^{n-1} ; \quad \Gamma = \sum_{\alpha=1}^{N_s} |\dot{\gamma}^\alpha| \quad (8)$$

where h_0 and n are hardening parameters, and Γ is the accumulated slip on all of the crystallographic slip systems. The material parameters, typically representative of aluminum alloys, used in the simulations are listed in Table 1.

2.2. Unit-cell formulation

Considering the spatial quasi-periodicity of the microstructure in polycrystalline metals, a unit-cell (UC) model subjected to periodic boundary conditions is selected to represent the bulk polycrystalline metals (for more details about the application of these boundary conditions, see Section 2.4). Furthermore, we assume the preexistence of microvoids, which are periodically distributed within the material. Thus, a cubic UC containing a single void at its center is considered. The initial void volume fraction f_0 is set to 4 %. The UC geometry is discretized, within ABAQUS 6.14 environment, by 5336 twenty-node hexahedral finite elements (C3D20 in ABAQUS terminology).

To highlight the influence of plastic anisotropy on ductile failure initiation, both single crystals and textured polycrystals are considered. Based on grain number sensitivity study (see Appendix A), each polycrystal contains 200 grains and is generated by the

¹ It is generally more suitable to use orthotropic elastic behavior considering the crystallographic symmetries inside the single crystals; however, the effect of elasticity on failure initiation is negligible, as the level of the limit strains is very high compared to the amount of elastic strain (see Ref. [39] for details). Thus, the elastic anisotropy effects can be disregarded in this study.

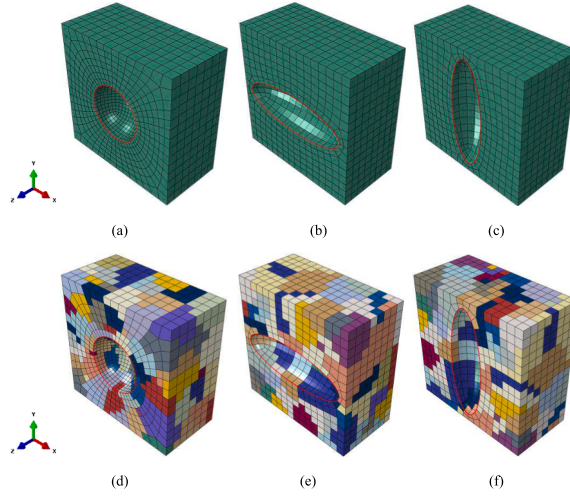


Fig. 1. Unit cells of single crystals containing (a) spherical ($w_0 = 1$), (b) oblate ($w_0 = 0.3$), and (c) prolate ($w_0 = 3$) voids; unit cells of polycrystalline aggregates containing (d) spherical ($w_0 = 1$), (e) oblate ($w_0 = 0.3$), and (f) prolate ($w_0 = 3$) voids.

Table 2
Crystallographic orientations and corresponding Euler angles.

orientation	φ_1 (deg)	Φ (deg)	φ_2 (deg)
[001]	0	0	0
[011]	-45	0	0
[123]	53	90	297

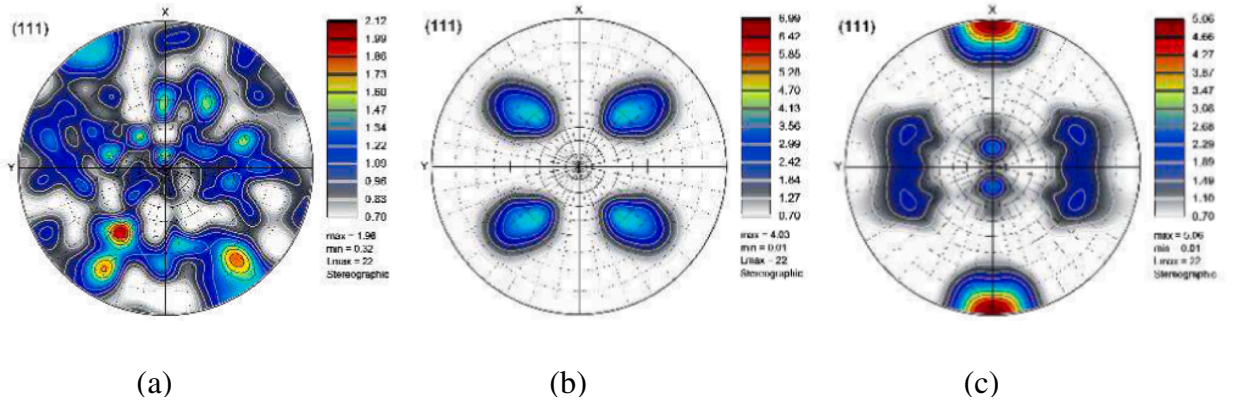


Fig. 2. Initial crystallographic textures in the form of (111) pole figures: (a) random; (b) cube; (c) copper.

Voronoi tessellation technique. The plastic anisotropy in this study is mainly due to the combined effects of initial void shape and crystallographic orientation. Thus, three initial void shapes are investigated: spherical ($w_0 = 1$), oblate ($w_0 = 0.3$, i.e., $r_{20}/r_{10} = r_{30}/r_{10} = 0.3$) and prolate ($w_0 = 3$, $r_{20}/r_{10} = r_{20}/r_{30} = 3$), where r_{i0} is defined as the i -th axial length of the void in the initial configuration. Fig. 1 displays the UCs of single crystals (Fig. 1a-c) and polycrystalline aggregates (Fig. 1d-f) containing voids with three different shapes. The three different crystallographic orientations and corresponding Euler angles used for single crystals are shown in Table 2. Also, three different crystallographic textures are used for polycrystalline aggregates: random (Ran.), cube (Cub.) component and copper (Cop.) component, as defined in Ref. [30]. The (111) pole figures corresponding to these textures are plotted in Fig. 2 using ATEX software [31].

2.3. Macroscopic loading

Two macroscopic loading configurations are considered in the UC computations: proportional triaxial stressing and proportional in-plane straining. The former is often used to investigate the effect of the stress triaxiality ratio and Lode parameter on the magnitude

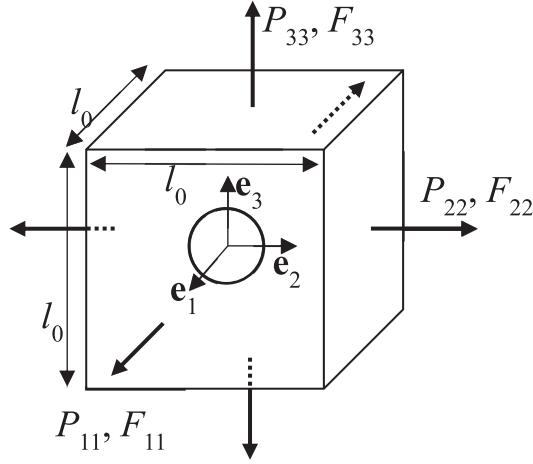


Fig. 3. Illustration of the triaxial macroscopic stress state.

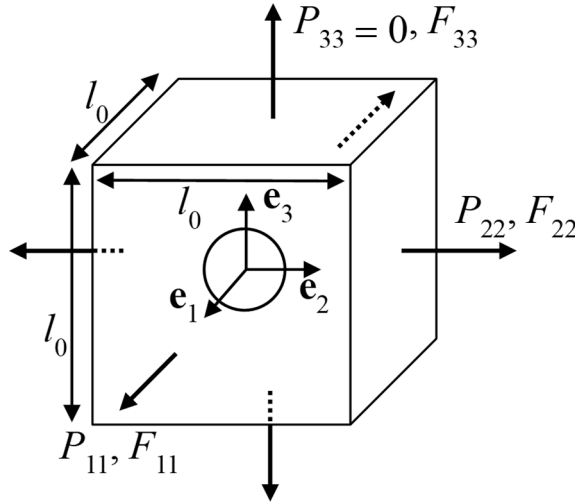


Fig. 4. Illustration of the macroscopic plane-stress state.

of the ductility limit strain. The latter configuration is classically applied in the prediction of forming limit curves of metal sheets. In this section, these two loading configurations are introduced by adopting the first Piola–Kirchhoff stress tensor \mathbf{P} (P_{ij} representing the ij -th component) and the deformation gradient \mathbf{F} (F_{ij} denoting the ij -th component) as work-conjugate stress and strain measures, respectively.

2.3.1. Proportional triaxial stressing

In this loading configuration, the UC undergoes a diagonal triaxial macroscopic stress state (see Fig. 3), i.e., only the diagonal components P_{11} , P_{22} , and P_{33} of the macroscopic stress tensor \mathbf{P} are nonzero (macroscopic shear stresses being neglected). Proportional triaxial stressing requires that the Cauchy stress ratios $\beta_1 = \Sigma_{11}/\Sigma_{33}$ and $\beta_2 = \Sigma_{22}/\Sigma_{33}$ are kept constant during the loading, where Σ_{11} , Σ_{22} and Σ_{33} refer to the diagonal components of the macroscopic Cauchy stress tensor Σ .

The mean stress Σ_m and the von Mises equivalent stress Σ_{eq} of the UC can be expressed as functions of β_1 and β_2 as:

$$\Sigma_m = \frac{\beta_1 + \beta_2 + 1}{3} \Sigma_{33}; \Sigma_{eq} = \frac{1}{\sqrt{2}} \sqrt{(\beta_1 - \beta_2)^2 + (\beta_1 - 1)^2 + (\beta_2 - 1)^2} |\Sigma_{33}| \quad (9)$$

Following the formulations adopted in [2] and [6], the macroscopic stress triaxiality T and Lode parameter L can be expressed in terms of the stress ratios β_1 and β_2 (assuming $\Sigma_{11} \geq \Sigma_{22} \geq \Sigma_{33}$) as follows:

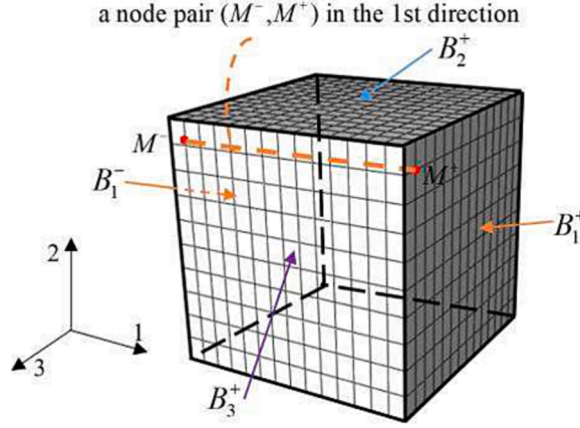


Fig. 5. Illustration of a node pair (M^-, M^+) constrained by PBCs.

$$\begin{cases} T = \frac{\Sigma_m}{\Sigma_{eq}} = \frac{\sqrt{2}(1 + \beta_1 + \beta_2)}{3\sqrt{(1 - \beta_1)^2 + (1 - \beta_2)^2 + (\beta_1 - \beta_2)^2}} \text{sgn}(\Sigma_{33}) \\ L = \frac{(2\beta_2 - \beta_1 - 1)}{\beta_1 - 1}, -1 \leq L \leq 1 \end{cases} \quad (10)$$

Constant stress ratios β_1 and β_2 during the deformation history result in a combination of constant T and L , which characterize the spherical and deviatoric parts of the macroscopic Cauchy stress tensor Σ , respectively. The numerical implementation of constant stress ratios is ensured by controlling the non-linear relations between the macroscopic strain components along the three loading directions.

2.3.2. Proportional in-plane straining

In this loading configuration, the UC undergoes a macroscopic plane-stress state (see Fig. 4), where the macroscopic fields are characterized as:

$$\mathbf{F} = \begin{pmatrix} F_{11} & 0 & \square \\ 0 & F_{22} & \square \\ \square & \square & \square \end{pmatrix}; \quad \mathbf{P} = \begin{pmatrix} \square & \square & 0 \\ \square & \square & 0 \\ 0 & 0 & 0 \end{pmatrix} \quad (11)$$

with the components F_{11} and F_{22} of the deformation gradient related to the strain components E_{11} and E_{22} by:

$$F_{11} = e^{E_{11}}; \quad F_{22} = e^{E_{22}} \quad (12)$$

Components ' \square ' in Eq. (11) are unknown and should be determined by FE computations. Then, the macroscopic loading is prescribed on the faces normal to the first ($x_{01} = \pm l_0/2$) and second ($x_{02} = \pm l_0/2$) spatial directions. On the other hand, faces normal to the third spatial direction are kept stress free (i.e., $P_{33} = 0$).

Proportional in-plane straining requires that the strain-path ratio $\rho = E_{22}/E_{11}$ is kept constant during plastic deformation. This strain-path ratio is varied between $-1/2$ and 1 to span a complete forming limit diagram (FLD).

2.4. Periodic boundary conditions

Fully periodic boundary conditions (PBCs) are applied to the unit cells via node-to-node constraints. Here, we detail the constraints on the pair of homologous nodes in the first spatial direction (direction 1). Extension to other spatial directions can be done in a very similar manner. A pair of nodes belonging to faces B_1^- and B_1^+ , which have identical coordinates in directions 2 and 3, is considered as illustrated in Fig. 5. The current positions of these two nodes are related to their initial positions by:

$$\mathbf{x}_{M^-} = \mathbf{F} \cdot \mathbf{x}_{0M^-} + \mathbf{u}_{M^-}^{per}; \quad \mathbf{x}_{M^+} = \mathbf{F} \cdot \mathbf{x}_{0M^+} + \mathbf{u}_{M^+}^{per} \quad (13)$$

where \mathbf{x} and \mathbf{x}_0 denote the current and initial positions of the considered node pair, respectively, \mathbf{F} is the deformation gradient, and \mathbf{u}^{per} is a periodic displacement field.

The PBCs imply that \mathbf{u}^{per} takes the same value for node pair (M^-, M^+) , i.e., $\mathbf{u}_{M^-}^{per} = \mathbf{u}_{M^+}^{per}$. Consequently, Eq. (13) can be recast in a more compact form:

$$\mathbf{x}_{M^+} - \mathbf{x}_{M^-} = \mathbf{F} \cdot (\mathbf{x}_{0M^+} - \mathbf{x}_{0M^-}) \quad (14)$$

This equation can be easily rewritten as:

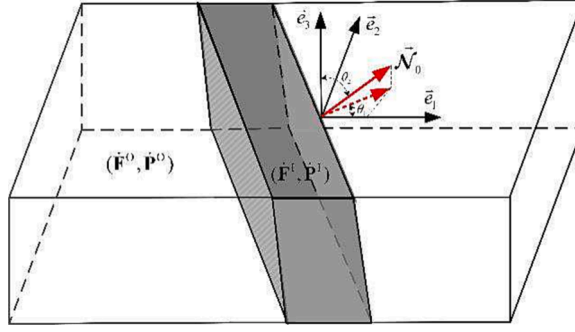


Fig. 6. Illustration of jump of mechanical fields across the discontinuity band.

$$\mathbf{u}_{M^+} - \mathbf{u}_{M^-} = (\mathbf{F} - \mathbf{I}) \cdot (\mathbf{x}_{0M^+} - \mathbf{x}_{0M^-}) \quad (15)$$

where $(\mathbf{u}_{M^-}, \mathbf{u}_{M^+})$ are the displacements of the nodes (M^-, M^+) , respectively.

Eq. (15) is imposed on the node pairs belonging to faces $\{B_1^-, B_1^+\}$ and $\{B_2^-, B_2^+\}$ in the loading configuration of proportional in-plane straining; while it is imposed on faces $\{B_1^-, B_1^+\}$, $\{B_2^-, B_2^+\}$ and $\{B_3^-, B_3^+\}$ in the loading configuration of proportional triaxial stressing. Numerical implementation of Eq. (15) is managed by the set of Python scripts *Homtools* [32]. More details about the practical aspects of implementation can be found in [2,33].

2.5. Ductile failure initiation criteria

In the present study, ductile failure initiation is marked by the occurrence of two events: plastic strain localization and void coalescence. The Rice bifurcation theory is used to predict the occurrence of plastic strain localization, while a strain-based criterion is employed to predict the onset of void coalescence. The formulations of these two criteria are briefly recalled in this section.

2.5.1. Plastic strain localization criterion

Following the Rice approach [20], the onset of plastic strain localization is triggered by a bifurcation associated with admissible jumps for strain and stress rates through a localization band (see Fig. 6). In a Lagrangian framework, the kinematic condition for the strain rate jump reads:

$$[[\dot{\mathbf{F}}]] = \dot{\mathbf{F}}^O - \dot{\mathbf{F}}^I = \dot{\mathbf{C}} \otimes \overline{\mathbf{N}} \quad (16)$$

where:

- $[[*]]$ denotes the jump of field $*$ across the localization band, and superscripts 'O' and 'I' represent quantity outside the band and its counterpart inside the band,
- $\dot{\mathbf{C}}$ is the jump vector,
- $\overline{\mathbf{N}}$ is the unit vector normal to the localization band, equal to $(\sin\theta_2 \cos\theta_1, \sin\theta_2 \sin\theta_1, \cos\theta_2)$, where $0 \leq \theta_1 \leq 2\pi$ and $0 \leq \theta_2 \leq \pi$.

The forces outside and inside the band satisfy the equilibrium condition, which can be expressed in a rate form as:

$$[[\dot{\mathbf{P}}]] \cdot \overline{\mathbf{N}} = \mathbf{0} \quad (17)$$

On the other hand, the constitutive equation at the macroscopic scale is formulated in a rate form as:

$$\dot{\mathbf{P}} = \mathbb{B} : \dot{\mathbf{F}} \quad (18)$$

where \mathbb{B} is the macroscopic elasto-plastic tangent modulus.

Combination of Eqs. (16), (17) and (18) leads to a jump kinematic condition as follows:

$$(\mathbb{B} : (\dot{\mathbf{C}} \otimes \overline{\mathbf{N}})) \cdot \overline{\mathbf{N}} = \mathbf{0} \quad (19)$$

which can be rewritten as:

$$(\mathcal{N}_i B_{ijkl} \mathcal{N}_l) \dot{\mathbf{C}}_k = 0 \quad (20)$$

By introducing a fourth-order tensor \mathbb{L} , which is obtained by permutation of the first and the second index of tensor \mathbb{B} (i.e., $\forall i, j, k, l: 1, 2, 3 : L_{ijkl} = B_{jikl}$), Eq. (20) becomes:

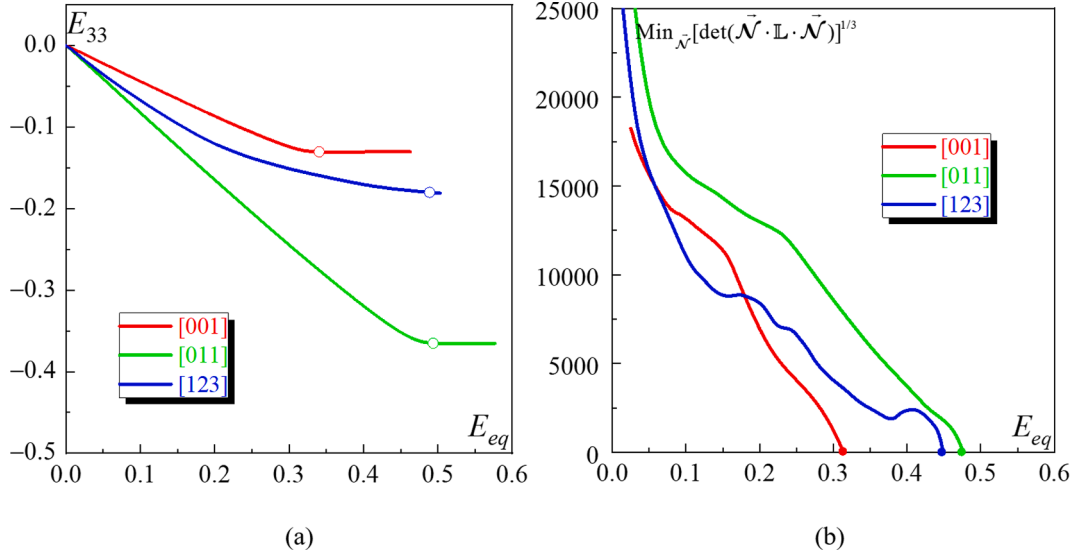


Fig. 7. Effect of crystallographic orientation on the evolution of: (a) E_{33} ; (b) $\text{Min}_{\vec{N}} [\det(\vec{N} \cdot \mathbb{L} \cdot \vec{N})]^{1/3}$ for single crystals with spherical void.

$$(\vec{N} \cdot \mathbb{L} \cdot \vec{N}) \cdot \dot{\vec{c}} = \vec{0} \quad (21)$$

Consequently, the occurrence of plastic strain localization corresponds to the singularity of the macroscopic acoustic tensor $\vec{N} \cdot \mathbb{L} \cdot \vec{N}$:

$$\det(\vec{N} \cdot \mathbb{L} \cdot \vec{N}) = 0 \quad (22)$$

The numerical detection of Eq. (22) can be treated as a minimization problem:

$$\text{minimize } \det(\vec{N} \cdot \mathbb{L} \cdot \vec{N}) \text{ for } 0 \leq \theta_1 \leq 2\pi \text{ and } 0 \leq \theta_2 \leq \pi \quad (23)$$

which is straightforwardly interpreted as: there is no plastic strain localization when the minimum of $\det(\vec{N} \cdot \mathbb{L} \cdot \vec{N})$ over all the band orientations (θ_1, θ_2) is strictly positive; by contrast, plastic strain localization occurs when the minimum of $\det(\vec{N} \cdot \mathbb{L} \cdot \vec{N})$ vanishes for the first time.

In order to check whether Eq. (22) is verified, tensor \mathbb{L} (defined as the analogous of the macroscopic elasto-plastic tangent modulus \mathbb{B}) should be provided at each increment of the FE computation. In the present work, the macroscopic tangent modulus \mathbb{B} is computed using the condensation technique originally proposed by Miehe [34]. The practical details regarding the implementation of this technique, in connection with the FE computation, can be found in Ref. [35].

It should be noted that the formulation presented in this subsection is directly applicable to triaxial macroscopic stress states. This formulation can be easily adapted to macroscopic in-plane stress states. The corresponding details can be found in Ref. [33], which are not repeated here for brevity.

2.5.2. Void coalescence criterion

In the present study, the strain-based criterion developed by Koplik and Needleman [23] and commonly used in the literature (see, e.g., Ref. [15] by Guo et al., and Ref. [16] by Ling et al.) is adopted to predict the onset of void coalescence. As stated by Koplik and Needleman [23], void coalescence arises at the moment when the strain state shifts from a general triaxial state to a uniaxial strain mode. With the convention adopted here, this condition is met when the strain rate components in the second and third spatial directions become zero:

$$\dot{E}_{22} = \dot{E}_{33} = 0 \quad (24)$$

This criterion is only relevant for triaxial macroscopic stress states, since void coalescence is not possible for in-plane stress states, when using the UC model adopted in the present work (see Ref. [2]).

3. Results and discussions

In this section, the combined effects of initial crystallographic orientation and void shape on strain localization and void

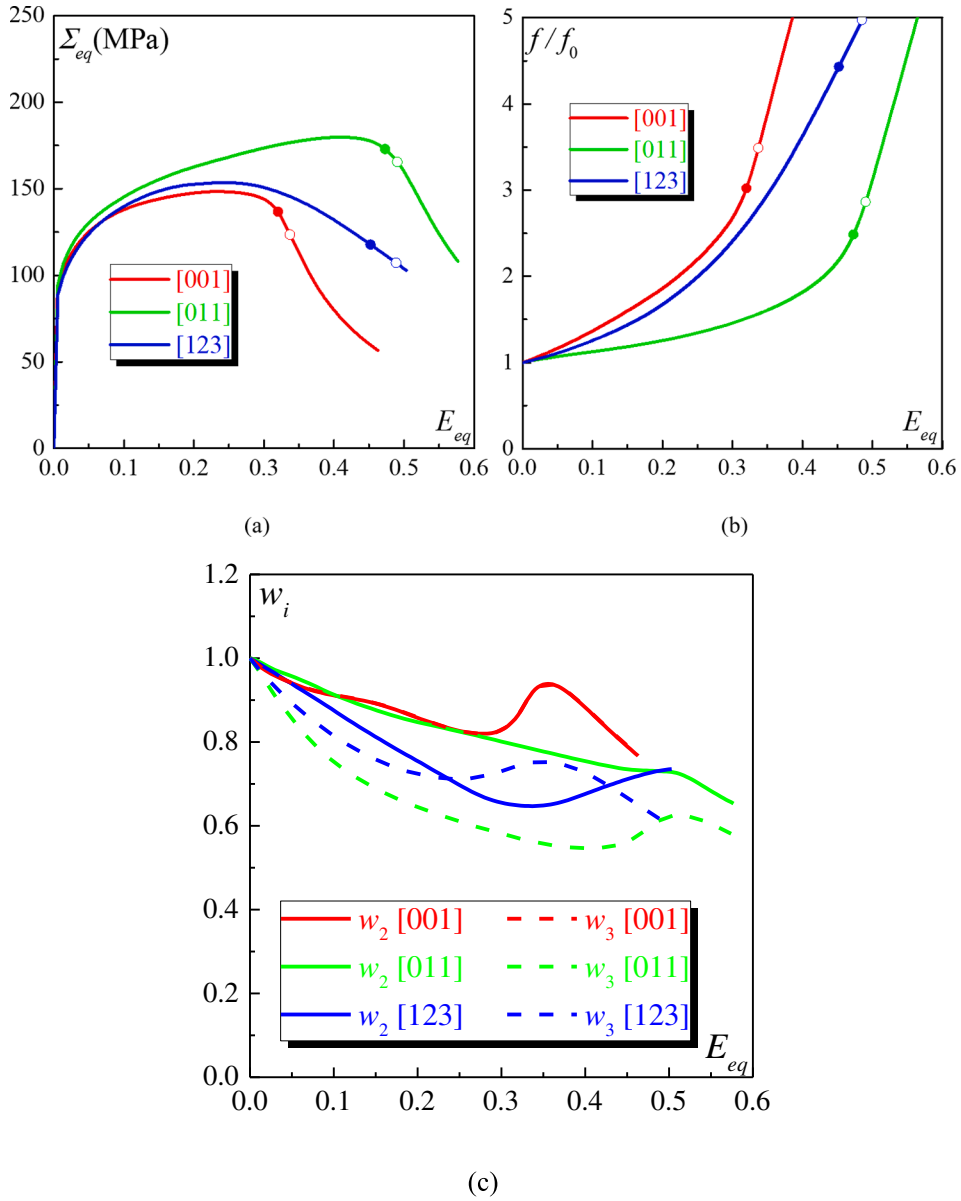


Fig. 8. Effect of crystallographic orientation on the evolution of the: (a) equivalent overall stress Σ_{eq} ; (b) normalized void volume fraction f/f_0 ; (c) void aspect ratios w_i , for single crystals with spherical void.

coalescence as well as on their competition are thoroughly discussed. Under proportional triaxial stressing, these combined effects are studied for both single crystals and polycrystalline aggregates. Under proportional in-plane straining, only forming limit diagrams (FLDs) corresponding to polycrystalline aggregates are analyzed, since FLDs of single crystals are not a common topic in plastic forming of metal sheets.

3.1. Voided single crystals under proportional triaxial stressing

The effect of crystallographic orientation on void coalescence in single crystals has been widely investigated in the literature [11,12,16,36]. The void shape effect on void coalescence in anisotropic solids using phenomenological models (rather than single crystal frameworks) has also been studied in [24]. However, the effects of crystallographic orientation and void shape on strain localization as well as their combined effects on void coalescence and strain localization in single crystals have not been sufficiently investigated yet, which represent the main focus of this section.

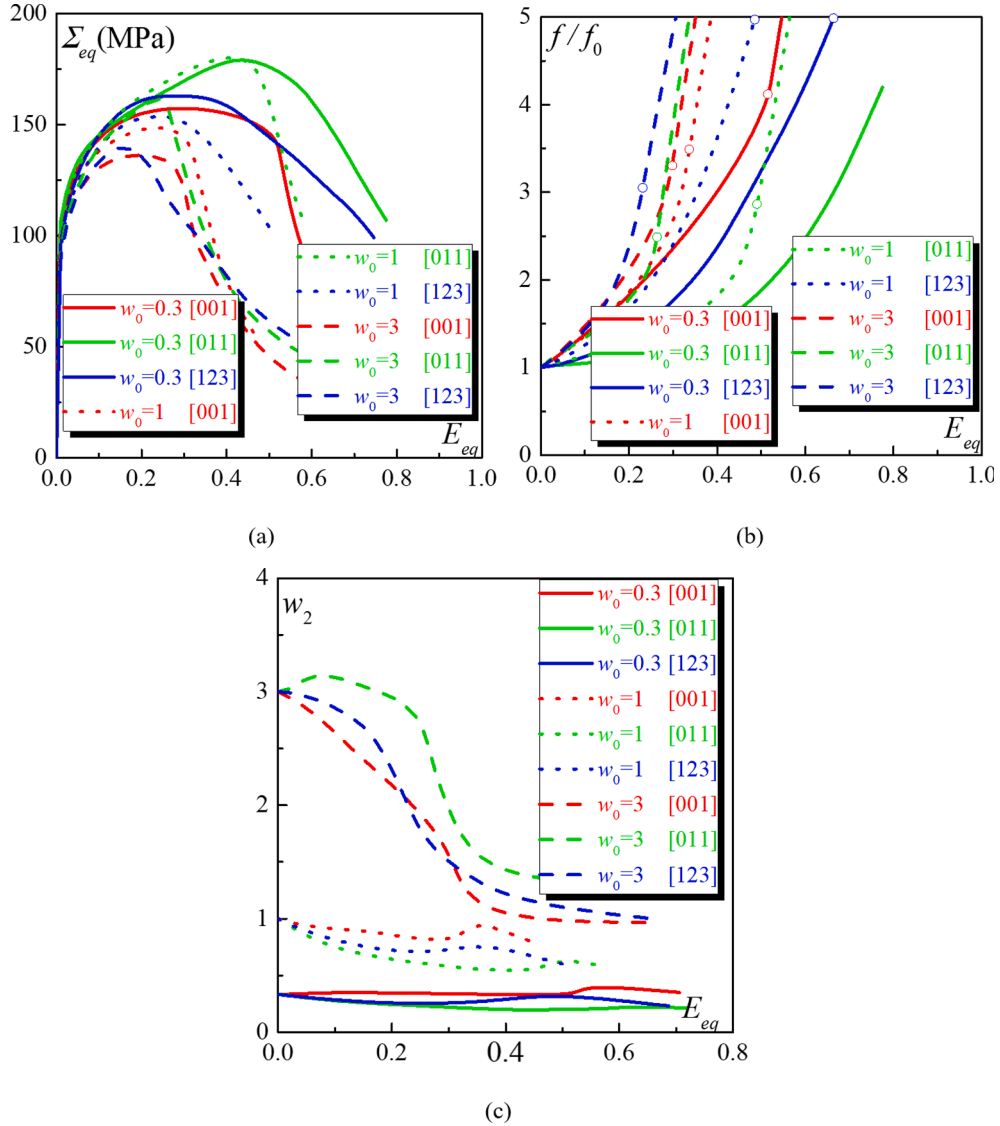


Fig. 9. Combined effect of crystallographic orientation and initial void shape on the: (a) equivalent overall stress Σ_{eq} ; (b) normalized void volume fraction f/f_0 ; (c) void aspect ratio w_2 , in single crystals.

3.1.1. Effect of crystallographic orientation

In this subsection, the effect of crystallographic orientation on failure initiation in single crystals with spherical void is examined. To this end, the three crystallographic orientations defined in Table 2 are considered. The stress triaxiality ratio T and the Lode parameter L are set to 1 and -1 , respectively.

Fig. 7a and b show the two indicators predicting the occurrence of void coalescence and plastic strain localization, respectively. The transition from void growth to coalescence stage is characterized by the transition of the deformation mode of the UC from triaxial to uniaxial, as marked by open circles in Fig. 7a. On the other hand, the incipience of strain localization is indicated by the vanishing of the minimum of determinant of the acoustic tensor $\vec{N} \cdot \mathbb{L} \cdot \vec{N}$ over all of the band orientations, as marked by full circles in Fig. 7b. The critical strains at the onset of void coalescence and strain localization are respectively denoted as E_{eq}^C and E_{eq}^B (where E_{eq} is the von Mises equivalent strain equal to $\frac{\sqrt{2}}{3} \sqrt{[(E_{11} - E_{22})^2 + (E_{22} - E_{33})^2 + (E_{33} - E_{11})^2]}$, as the off-diagonal strain components are equal to zero), which are used as measures of the ductility limit throughout the following sections of this paper.

It can also be seen from Fig. 7 that the ductility limit strain for orientation [011] is the highest, followed by [123] and then [001] orientation. The dependence of the ductility limit strain to the initial crystallographic orientation is obvious. Indeed, even if the applied loading is the same, the difference in the initial crystallographic orientation induces a difference in the activity of crystallographic slip systems and then a significant difference in the plastic deformation and mechanical response. This result confirms the strong

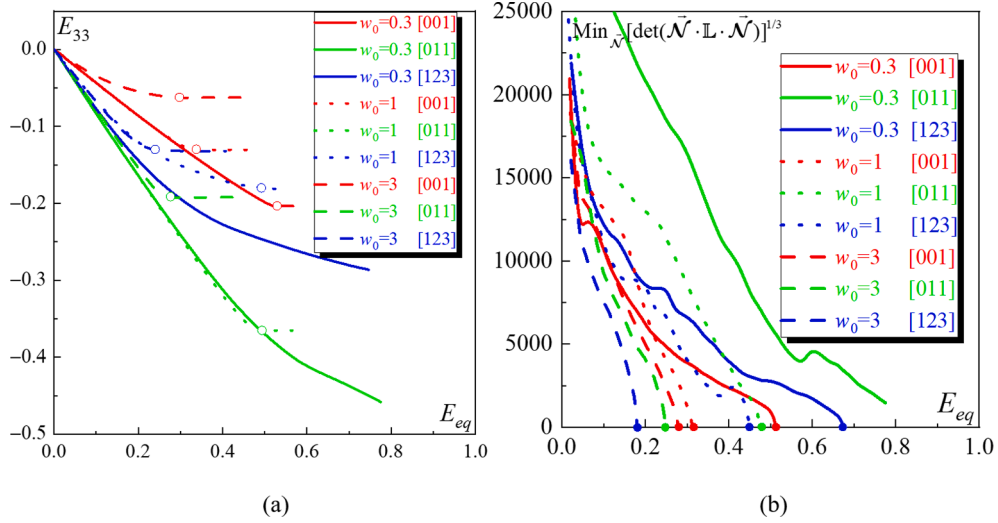


Fig. 10. Combined effect of initial void shape and crystallographic orientation on the evolution of: (a) E_{33} ; and (b) $\text{Min}_{\vec{N}} [\det(\vec{N} \cdot \mathbf{L} \cdot \vec{N})]^{1/3}$, in single crystals.

anisotropy of the ductile failure of single crystals.

The stage of ductile failure initiation is accompanied by several remarkable phenomena: a rapid drop in the stress carrying capacity of the UC, as revealed by Fig. 8a (where the evolution of the von Mises equivalent stress Σ_{eq} is plotted versus the equivalent strain E_{eq}), an acceleration of the void growth, as shown in Fig. 8b (where the evolution of the void volume fraction f , normalized by its initial value f_0 , is plotted against E_{eq}), and a significant change in the void aspect ratio, as highlighted in Fig. 8c. As can be seen in Fig. 8a, [001]-oriented UC presents the earliest loss of stress carrying capacity (softening), followed by [123] and then [011]-oriented UC. This result can be explained by the fact that the [001]-orientation yields the fastest void growth, followed by [123] and then [011] orientation, as revealed by Fig. 8b. Fig. 8c shows the evolution of the void aspect ratios $w_2 = r_2/r_1$ (with r_i being the i -th axial length of the deformed void) and $w_3 = r_3/r_1$. As can be seen in Fig. 8c, the evolutions of w_2 and w_3 for UC with [001]-orientation are coincident with each other (see the red curves). This is quite expected due to the fact that for orientation [001], the mechanical responses along the three principal directions are the same. By contrast, for [011]-orientation (plotted by green curves), the evolution of w_2 and w_3 are distinct from each other, thus indicating the strong plastic anisotropy along the second and third spatial directions of the UC. Specifically, the void expands more intensely along the second spatial direction as compared to the third one. The evolutions of w_2 and w_3 for orientation [123] are intersected with each other (see blue curves), thus suggesting a significant void rotation during plastic deformation. Based on Fig. 8a and b, it is also observed that E_{eq}^C is larger than E_{eq}^B for all three orientations, and their difference is dependent on the initial crystallographic orientation. This dependency will be further discussed in Section 3.1.3.

In fact, the orientation effect in single crystals can be interpreted as the effect of the loading direction with respect to the crystallographic axes, which would be referred to in terms of the crystallographic direction of the maximum principal stress component [15]. In our case, the maximum principal stress component is assumed to be parallel to the first UC spatial direction (i.e., x_1 , see Section 2.3.1). It is noted that different crystallographic directions of the maximum principal stress can lead to different mechanical responses for the same non-cubic orientation, such as [123]-orientation.

3.1.2. Combined effect of crystallographic orientation and void shape

Focus is confined in this subsection on the combined influence of initial void shape and crystallographic orientation on ductile failure initiation. The combined influence on the evolution of the equivalent overall stress Σ_{eq} , the void growth f , and the void aspect ratio w_2 is respectively depicted in Fig. 9a, b, and c. In each figure, curves of 9 cases are plotted against the equivalent strain E_{eq} : three crystallographic orientations {[001], [011], and [123]} \times three initial void shapes $\{w_0 = 0.3, 1, \text{ and } 3\}$. For these simulations, the stress triaxiality ratio T and the Lode parameter L are set to 1 and -1 , respectively. As can be seen from Fig. 9a, whatever the crystallographic orientation, void shapes $w_0 = 0.3$ and $w_0 = 3$ yield respectively the highest and the lowest resistance to material softening. This is due to the fact that aspect ratio $w_0 = 0.3$ leads to the slowest void growth rate, and aspect ratio $w_0 = 3$ yields the fastest void growth rate, as shown in Fig. 9b. This trend can also be validated by Fig. 9c, where the aspect ratio w_2 for the case $w_0 = 3$ decreases significantly with increasing the applied strain, thus leading to a significant change in the void shape and volume. By contrast, for the case $w_0 = 0.3$, w_2 exhibits only a slight change during plastic deformation, thus suggesting a relatively small change in the void shape and volume. On the other hand, Fig. 9b shows that, for $w_0 = 0.3$, the orientation [001] leads to the fastest void growth, followed by [123] and then [011]. This trend is the same as that observed for $w_0 = 1$, but different from that revealed for $w_0 = 3$. In the case of $w_0 = 3$, the [123]-oriented UC has the fastest void growth. This means that the orientation effect on the void growth is dependent on the void shape. Thus, the void growth rate is determined by the combined effect of crystallographic orientation and void shape. The void

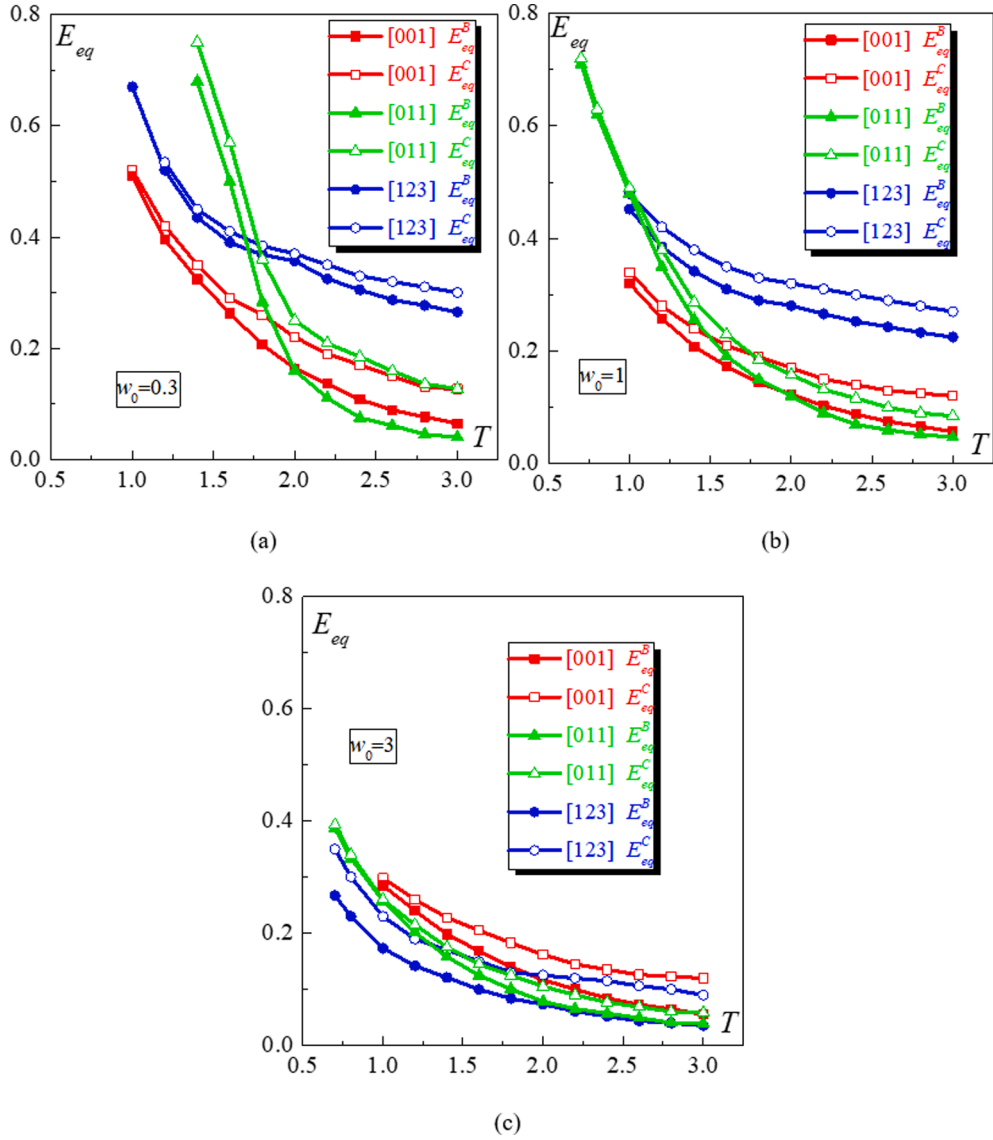


Fig. 11. Evolution of the limit strains E_{eq}^C and E_{eq}^B for the void shape: (a) $w_0 = 0.3$; (b) $w_0 = 1$; (c) $w_0 = 3$, in single crystals.

growth induced ductile failure initiation is also expected to be affected by this combined effect.

The combined influence of initial void shape and crystallographic orientation on the two above-discussed ductility indicators (namely the strain component E_{33} and the minimum of the determinant of the acoustic tensor $\vec{N} \cdot \mathbb{L} \cdot \vec{N}$) is respectively depicted in Fig. 10a and b. As can be seen from Fig. 10, the void shape effect on the limit strain is preserved for a given orientation². However, the orientation effect is not always maintained for a given void shape. These observations are already reflected in the plots of the equivalent stress-strain responses shown in Fig. 9a as well as in the plots of the void growth rate shown in Fig. 9b. The comparison between Fig. 10a and Fig. 10b reveals that the trends obtained for the onset of void coalescence are generally consistent with those observed for the incipience of strain localization. The detailed quantitative competition between these two events will be discussed in the next subsection.

3.1.3. Competition between strain localization and void coalescence

To further analyze the competition between void coalescence and plastic strain localization over a wide range of triaxiality ratios,

² Note that, for void shape $w_0 = 0.3$, the limit strains in the case of orientation [0 1 1] are not obtained by the UC computation, due to some convergence problems caused by too large plastic deformation. This issue may be solved by some numerical techniques, such as adaptive remeshing, but which is not pursued here since the presented trends are already clear.

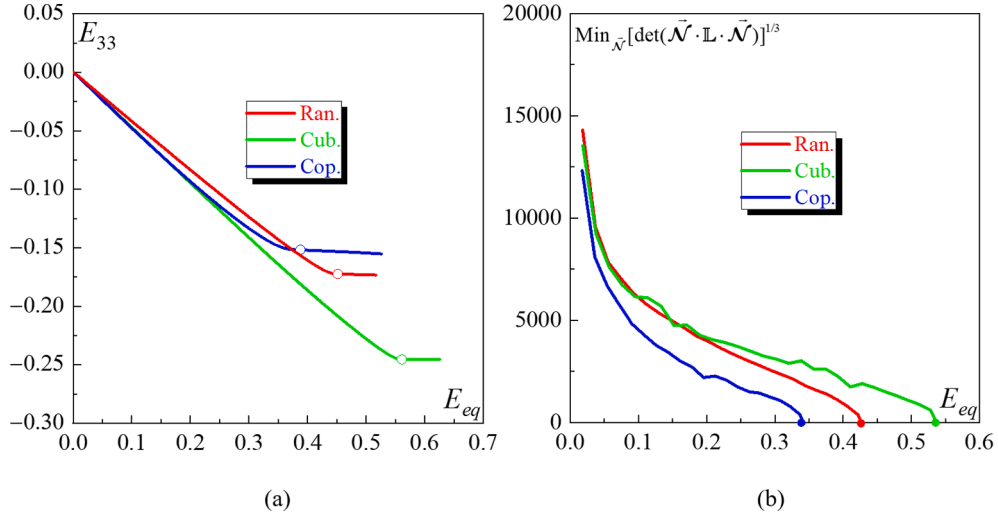


Fig. 12. Effect of crystallographic texture on the evolution of: (a) E_{33} ; (b) $\text{Min}_{\vec{N}} [\det(\vec{N} \cdot \mathbf{L} \cdot \vec{N})]^{1/3}$ for polycrystals with spherical void.

the evolutions of the corresponding limit strains E_{eq}^C and E_{eq}^B against T are plotted in Fig. 11. As revealed by Fig. 11a, for $w_0 = 0.3$, orientation [011] yields the largest limit strains when $T < 1.75$, while orientation [123] yields the highest limit strains when $T > 1.75$. Similar trends are found for $w_0 = 1$, as shown in Fig. 11b: orientation [011] yields the largest limit strains when $T < 1$, while orientation [123] yields the highest limit strains when $T > 1$. These trends are different from those observed for $w_0 = 3$ (see Fig. 11c), where it was found that the [001]-orientated crystal has the highest limit strains. Globally, the level of limit strains for a given orientation in the case $w_0 = 0.3$ is very sensitive to the change in the triaxiality ratio T , especially for orientation [011]. This sensitivity becomes weaker as w_0 increases. This observation can be attributed to the fact that the void shape $w_0 = 0.3$ (oblate) and the low stress triaxiality ratio are inherently unfavorable to void growth. Therefore, $w_0 = 0.3$ under low stress triaxiality yields a very slow void growth rate and accordingly high limit strains.

It is clearly shown from Fig. 11a-c that E_{eq}^C is always larger than E_{eq}^B , and the difference between them generally increases as T increases. The sensitivity of this difference to the stress triaxiality ratio is dependent on both the crystallographic orientation and the void shape. For example, in the case of $w_0 = 3$, the difference between E_{eq}^C and E_{eq}^B for orientation [011] is the smallest, and it can be neglected when $T < 1$. However, the difference between E_{eq}^C and E_{eq}^B for orientation [123] is the largest, so that the loci of E_{eq}^C and E_{eq}^B are absolutely separate over the whole range of T . Compared to the situation when $w_0 = 3$, the difference between E_{eq}^C and E_{eq}^B for orientation [011] in the case of $w_0 = 0.3$ is the largest among the three orientations. This means that the difference between E_{eq}^C and E_{eq}^B for a given orientation is significantly influenced by the void shape.

Based on the observations in Fig. 11, some statements can be made for voided single crystals. The orientation effect on void coalescence and strain localization is affected by the initial void shape and, conversely, the effect of initial void shape on void coalescence and strain localization is influenced by the crystallographic orientation. This observation is evident as the initial void shape affects the orientation evolution, which in turn affects the void evolution. Thus, the combined effect induced by the void shape and crystallographic orientation dictates the loci of the two limit strains predicted by void coalescence and strain localization. In general, strain localization takes place earlier than void coalescence. The difference between the two limit strains generally increases with increasing the stress triaxiality ratio T . The sensitivity of this difference to the magnitude of T is highly dependent on the combined effect of crystallographic orientation and void shape. In fact, the combined effect can be interpreted as the combined contribution to plastic anisotropy resulting from the initial void shape and crystallographic orientation.

3.2. Voided polycrystalline aggregates under proportional triaxial stressing

Crystallographic texture, often observed in rolled metal sheets, is an important feature of anisotropic plastic behavior, and has been demonstrated to play a major role in ductile failure initiation [37]. In this subsection, the effects of crystallographic texture and void shape on void coalescence and strain localization are investigated for polycrystalline aggregates.

3.2.1. Effect of crystallographic texture

The texture effect is firstly examined in polycrystalline aggregates with spherical void. To this end, the three textures introduced in Section 2.2 (namely, Ran., Cub. and Cop.) are considered. The stress triaxiality ratio and Lode parameter are set to 0.7 and -1 , respectively. Fig. 12 shows the evolution of the strain component E_{33} and $\text{Min}_{\vec{N}} [\det(\vec{N} \cdot \mathbf{L} \cdot \vec{N})]^{1/3}$ for the three textures, which are the indicators of the onset of void coalescence and strain localization. It can clearly be seen from Fig. 12a that Cub. texture leads to the

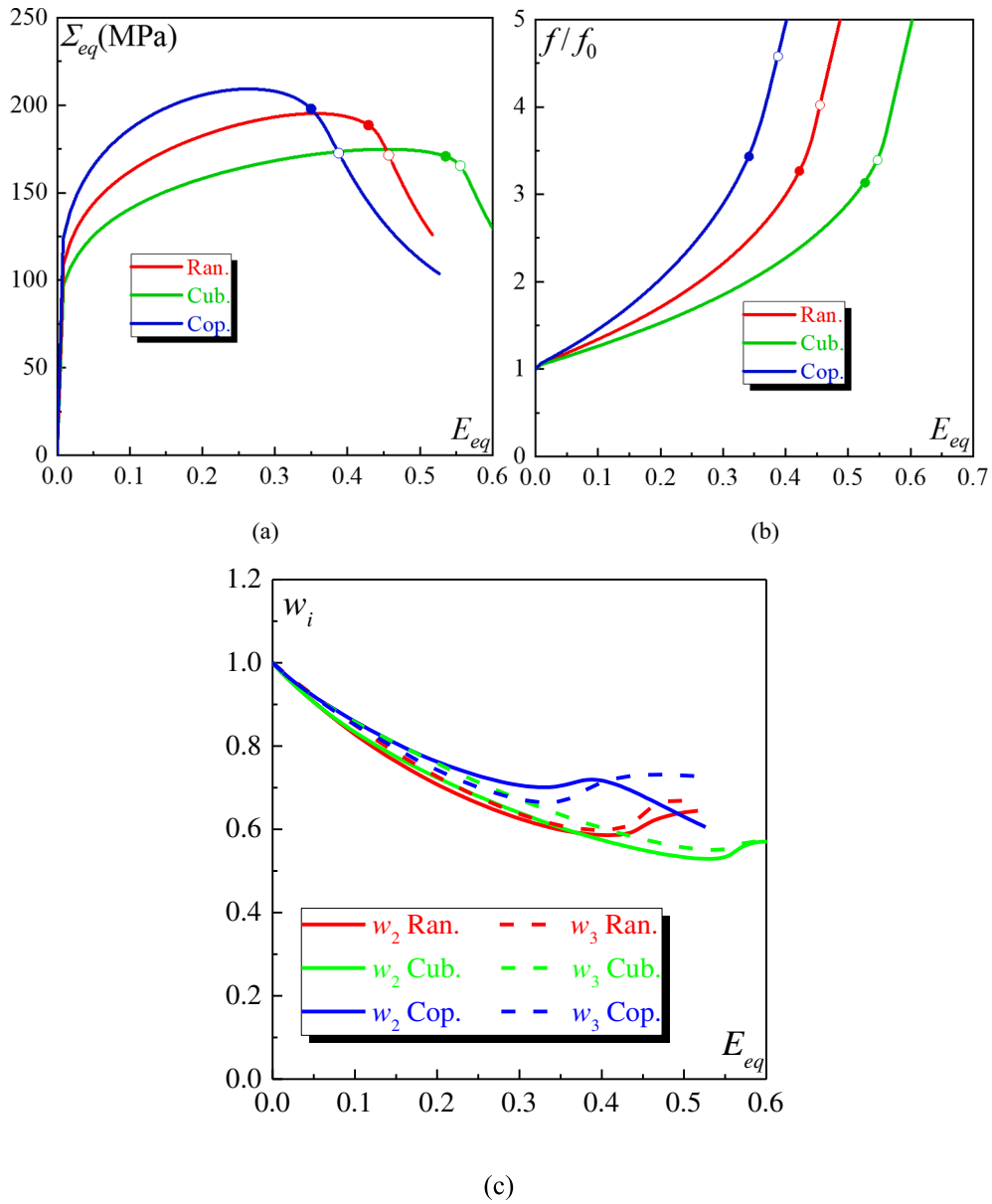


Fig. 13. Effect of crystallographic texture on the evolution of the: (a) equivalent overall stress Σ_{eq} ; (b) normalized void volume fraction f/f_0 ; (c) void aspect ratios w_i , for polycrystals with spherical void.

highest E_{eq}^C followed by Ran. and then Cop. This texture effect is consistently reproduced for E_{eq}^B , as revealed by Fig. 12b. Meanwhile, Cub. (resp. Cop.) texture yields the slowest (resp. fastest) softening of the overall stress–strain response due to the slowest (resp. fastest) void growth, as clearly shown in Fig. 13a and b. These predictions are consistent with the results obtained by Bryhni Dæhli et al. [25], and clearly explain the trends on the limit strain levels in Fig. 12. The onsets of void coalescence and strain localization are also marked and compared in Fig. 13a and b, which suggest that the difference between the corresponding limit strains E_{eq}^C and E_{eq}^B is evidently dependent on the crystallographic texture (this aspect will be further discussed in Section 3.2.3). Fig. 13c shows the evolution of the void aspect ratios w_i for the three textures. As can be clearly seen, the evolutions of w_2 and w_3 for Ran. texture present only a slight difference, thus indicating that the UC with Ran. texture does not exhibit apparent plastic anisotropy. Based on the evolutions of w_i for Cub. and Cop. texture, it can be readily observed that the matrix anisotropy has a pronounced effect on the resulting void shape evolution.

3.2.2. Combined effect of crystallographic texture and void shape

The combined influence of initial void shape and crystallographic texture on the evolution of the equivalent stress Σ_{eq} , void growth

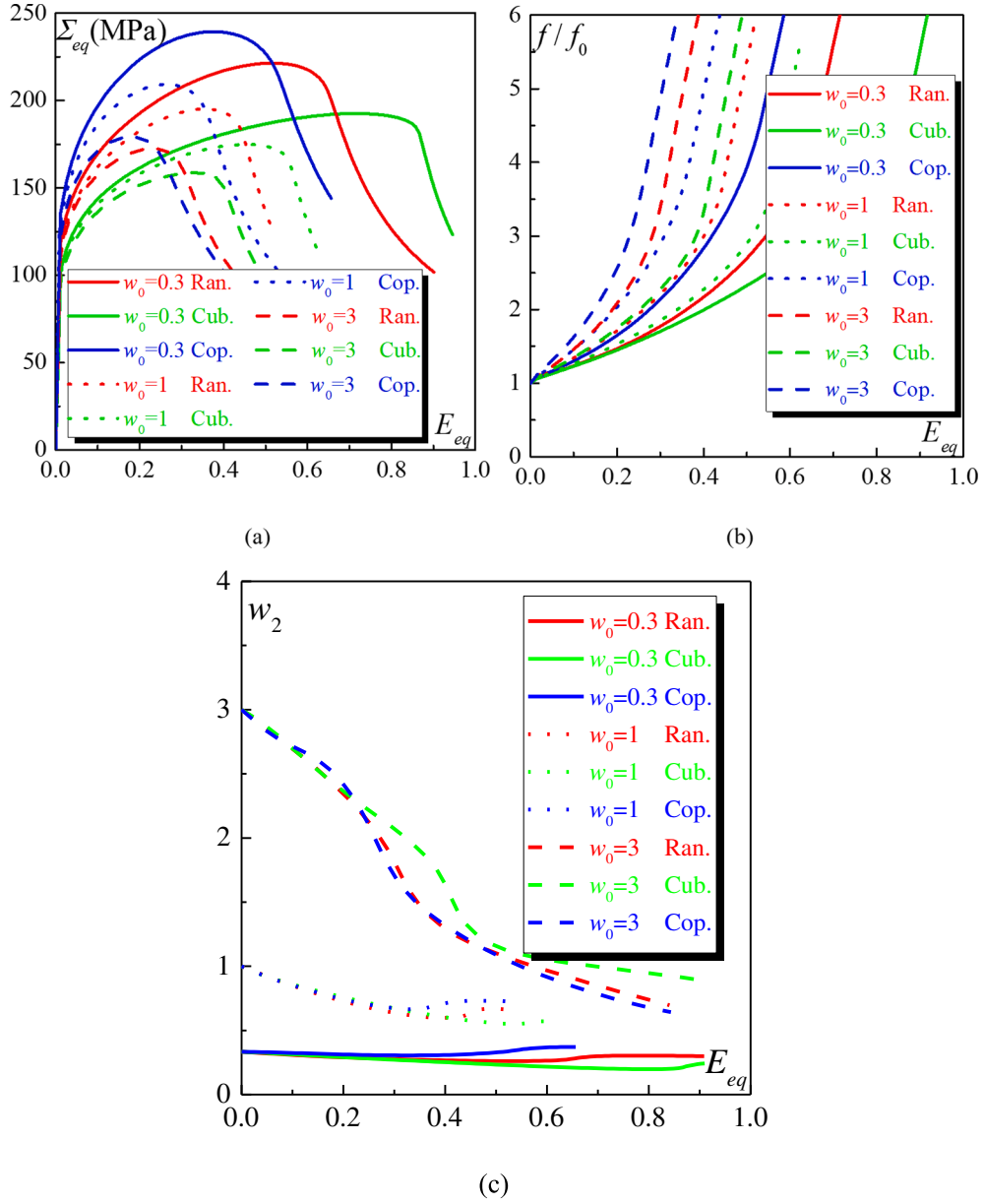


Fig. 14. Combined effect of crystallographic texture and initial void shape on the: (a) equivalent overall stress Σ_{eq} ; (b) normalized void volume fraction f/f_0 ; (c) void aspect ratio w_2 , in single crystals.

f , and void aspect ratio w_2 is respectively depicted in Fig. 14a, b, and c, where the curves of 9 cases are plotted at $\{T = 0.7, L = -1\}$: three crystallographic textures {Ran., Cub., and Cop.} \times three void shapes $\{w_0 = 0.3, 1, \text{ and } 3\}$. As can clearly be seen in Fig. 14a and b, for a given crystallographic texture, void shape $w_0 = 0.3$ (resp. $w_0 = 3$) always leads to the strongest (resp. weakest) resistance to material softening and slowest (resp. fastest) void growth rate. The void shape effect is similar to that observed in single crystals. For a given void shape, Cub. texture (resp. Cop. texture) always leads to the strongest (resp. weakest) resistance to material softening and slowest (resp. fastest) void growth rate. In other words, the texture effect is maintained regardless of the void shape. This is not similar to what has been observed for single crystals, where the orientation effect can be reversed depending on the void shape. In addition, compared to the other two void shapes, the texture effect for void shape $w_0 = 0.3$ seems to be more pronounced than for the other void shapes. As shown in Fig. 14c, unlike the orientation effect on void shape evolution in single crystals, the texture effect on void shape evolution in polycrystals for a given initial void shape is relatively moderate, especially when $E_{eq} < 0.25$. This can be well understood since the different oriented grains in polycrystalline aggregates accommodate and coordinate the applied loading. However, as plastic deformation increases, the different matrix heterogeneity induced strain concentration will be accumulated in certain places of the void surface, thus leading to significantly different void shape evolution.

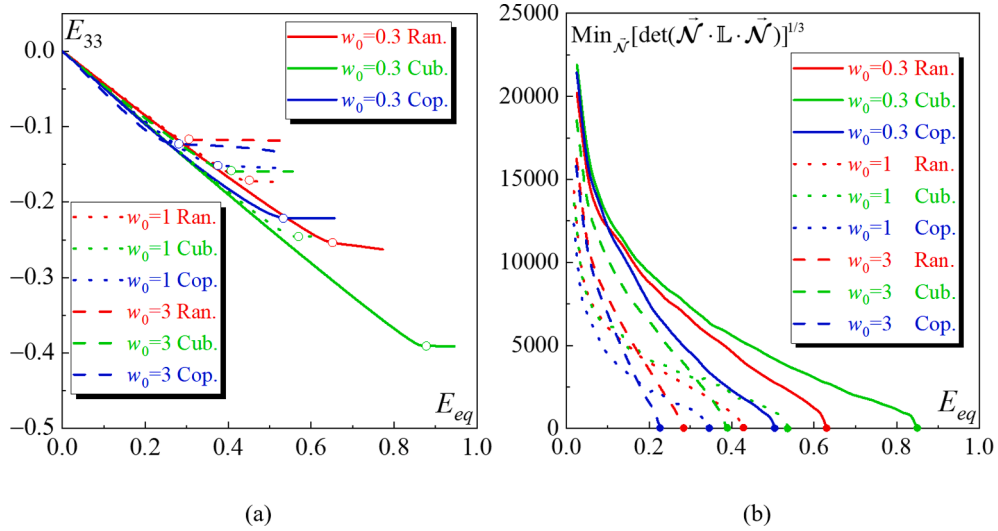


Fig. 15. Combined effect of initial void shape and crystallographic texture on the evolution of: (a) E_{33} and (b) $\text{Min}_{\vec{N}}[\det(\vec{N} \cdot \mathbb{L} \cdot \vec{N})]^{1/3}$ for polycrystals.

The influences of initial void shape and crystallographic texture on the evolution of E_{33} and $\text{Min}_{\vec{N}}[\det(\vec{N} \cdot \mathbb{L} \cdot \vec{N})]^{1/3}$ are respectively depicted in Fig. 15a and b. As can clearly be seen from Fig. 15, the texture effect on the limit strain of a polycrystal is preserved regardless of the void shape and, conversely, the void shape effect is maintained regardless of the texture. These observed trends are already reflected in the equivalent stress–strain responses shown in Fig. 14a and in the void growth rate shown in Fig. 14b.

3.2.3. Competition between strain localization and void coalescence

To quantitatively study the combined effect of void shape and initial texture over a wide range of triaxiality ratios, we plot in Fig. 16 the evolutions of the two limit strains E_{eq}^B and E_{eq}^C against T , corresponding to the three crystallographic textures and three void shapes. Based on the trends revealed by Fig. 16a-c, the following conclusions can be drawn for voided polycrystals:

- For relatively low stress triaxiality, the two limit strains are almost equal to each other, thus indicating that void coalescence and strain localization occur simultaneously. However, for relatively high stress triaxiality, E_{eq}^C is larger than E_{eq}^B , thus suggesting that strain localization acts as precursor to void coalescence. These trends are independent of the initial void shape and crystallographic texture. Nonetheless, the stress triaxiality level at which the two limit strains become distinct is indeed dependent on the initial void shape and crystallographic texture. For example, in the case of $w_0 = 0.3$, the two limit strains become distinct at $T = 1.2$ for Cub. texture, $T = 1$ for Ran. texture, and $T = 0.8$ for Cop. texture. This result further confirms that the stress triaxiality effect on the difference between the two limit strains is closely associated with plastic anisotropy, which has not been observed by other authors studying the competition between these two mechanisms (see, e.g., Ref. [1] by Tekoğlu et al., and Ref. [2] by Zhu et al.).
- It is clear that, for a given texture, the limit strains are most sensitive to the change in stress triaxiality T (ranging from 0.7 to 3) when $w_0 = 0.3$, followed by $w_0 = 1$, and then $w_0 = 3$. This trend is similar to that observed for single crystals, and is dominated by the void shape. On the other hand, the difference between the limit strains induced by the texture effect is more significant at low stress triaxiality when $w_0 = 0.3$. This implies that the texture effect may be more important at low stress triaxiality for $w_0 = 0.3$ than for the other two void shapes. The void shape is an important factor, which contributes to plastic anisotropy in addition to the impact of crystallographic texture.

3.3. Voided polycrystalline aggregates under proportional in-plane straining

The formability of metal sheets is influenced by some key factors, such as material hardening parameters and plastic anisotropic behavior. It has been demonstrated in the literature that the hardening parameters mainly affect the left-hand side of the forming limit diagrams (FLDs) [33], while the anisotropic behavior strongly affects the right-hand side of the FLDs [38]. In this subsection, focus is restricted to the combined anisotropic effects, which are due to crystallographic texture and void shape, on material formability. The UCs are undergoing proportional in-plane straining loadings (as introduced in Section 2.3.2).

In this macroscopic loading configuration, the strain components E_{11} and E_{22} are kept proportional for a prescribed strain-path ratio $\rho = E_{22}/E_{11}$, while E_{33} is determined by the plane-stress condition ($\Sigma_{33} = 0$). This stress state can also be characterized by a couple of T and L (defined by Eq. (10)). For instance, the stress state corresponding to $\rho = -0.5$ is near uniaxial tension, for which the average values of $\{T, L\}$ are around $\{0.3, -1\}$, as shown in Fig. 17a. Such a low stress triaxiality level does not lead to significant void growth, as

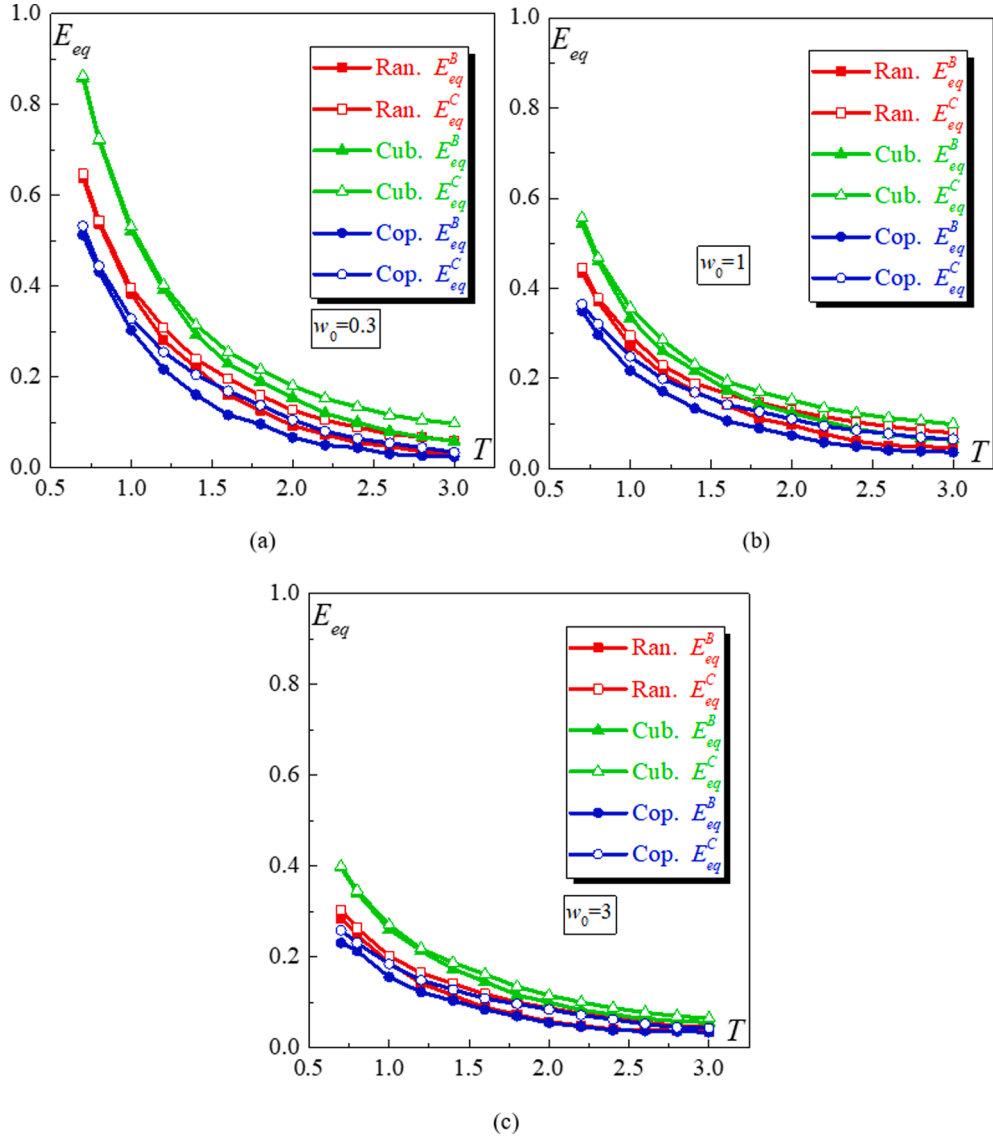


Fig. 16. Evolution of the limit strains E_{eq}^C and E_{eq}^B against T for the three void shapes in polycrystalline aggregates: (a) $w_0 = 0.3$; (b) $w_0 = 1$; (c) $w_0 = 3$.

revealed by Fig. 17b. Moreover, Fig. 17b suggests that ductile failure initiation in the considered loading configuration cannot be detected by void coalescence, since $\rho > 0$ leads to relatively larger void growth than $\rho = 0$, while $\rho > 0$ generally yields relatively higher limit strain than $\rho = 0$ (which will be validated by Fig. 18). In fact, the deformation mode transition does not occur owing to the nature of applied macroscopic loading, i.e., E_{11} and E_{22} are prescribed to evolve monotonically, while E_{33} consequently decreases. Whether void coalescence can be reached is dependent on the stress state inside the UC and also on the mechanical behavior of regions surrounding this UC. It has been demonstrated in Ref. [2] that the deformation mode transition can be obtained in this loading configuration by adopting a dense sheet with a narrow voided band (see Ref. [2] for more details). Thus, void coalescence in the state of proportional in-plane straining is not predicted by the proposed strain-based criterion. Consequently, ductile failure initiation (represented in the form of FLD) in this subsection is predicted only by plastic strain localization.

The effect of the combined anisotropy sources on the FLD predictions is depicted in Fig. 18. It is revealed that, for a given void shape, the texture effect on formability is relatively small for $\rho < 0$, almost negligible for $\rho = 0$, and much more significant for $\rho > 0$. These trends are consistent with those observed in Refs. [37] and [29]. It is also observed that, for a given initial texture, the initial void shape affects the level of forming limits for all the strain paths. This is in some variance with the results presented in Ref. [2], where the void shape was found to only affect the right-hand side of the FLDs, mainly due to the use of an isotropic phenomenological model. In the current investigation, however, the interaction between texture and void shape evolution results in perceptible differences in the macroscopic hardening behavior of the different UCs studied in Fig. 18 (even if their microscopic hardening parameters are the same).

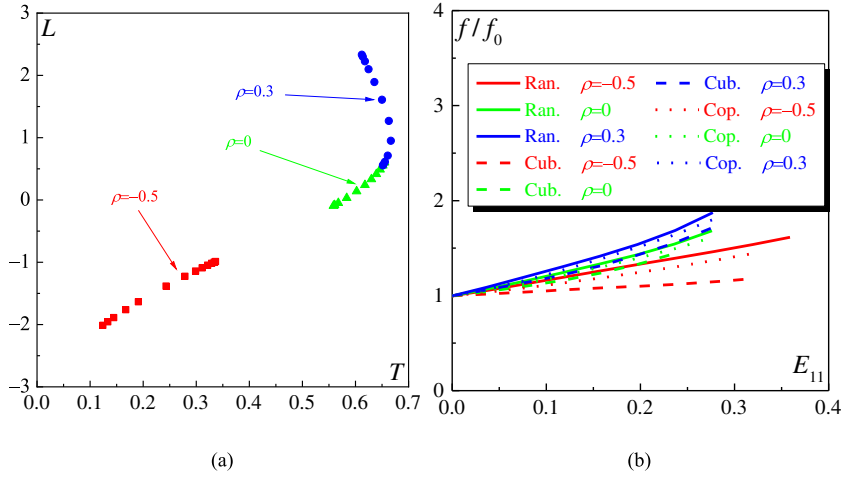


Fig. 17. Study of strain-path ratios $\rho = -0.5, 0, 0.3$: (a) T - L maps; (b) normalized void volume fraction f/f_0 for polycrystals with spherical void.

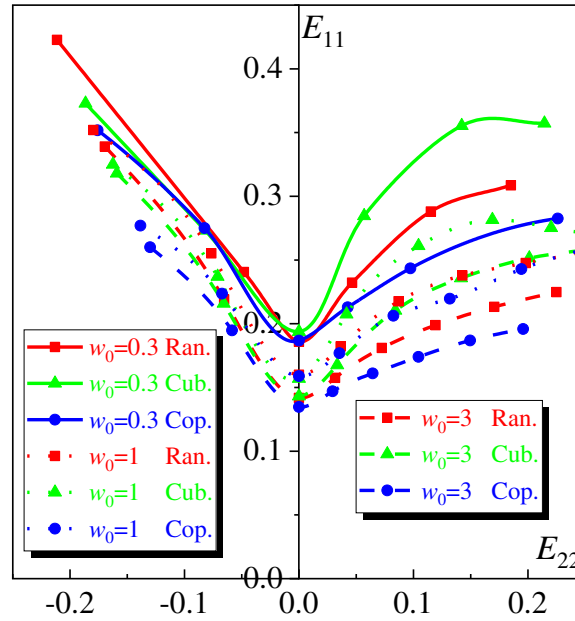


Fig. 18. Combined effect of initial void shape and crystallographic texture on the FLDs.

These induced differences impact in turn the predicted limit strains in the range of negative strain-path ratios. Such effects have not been taken into account in Ref. [2], where the behavior of the metal matrix was assumed to be isotropic. More interestingly, in the range of positive strain-path ratios, the ductility limit increases as the void aspect ratio w_0 decreases. This result is due to the fact that the void with aspect ratio $w_0 = 3$ grows faster than the two others, as shown in Fig. 10a and Fig. 15a. Consequently, the ductility of the corresponding UC is negatively affected by this more significant void growth.

4. Conclusions

In the present paper, the anisotropic effects, induced by both grain orientation and void shape, on plastic strain localization and void coalescence have been investigated using UC computations based on CPFEM. The investigations are conducted for both single crystals and textured polycrystals. Specifically, strain localization in this study is predicted by the bifurcation analysis within a multiscale periodic homogenization scheme. To cover a wide range of stress states, the simulations are performed under two macroscopic loading configurations: proportional triaxial stressing, characterized by constant stress triaxiality and Lode parameter, and proportional in-plane straining, specified by constant strain-path ratios.

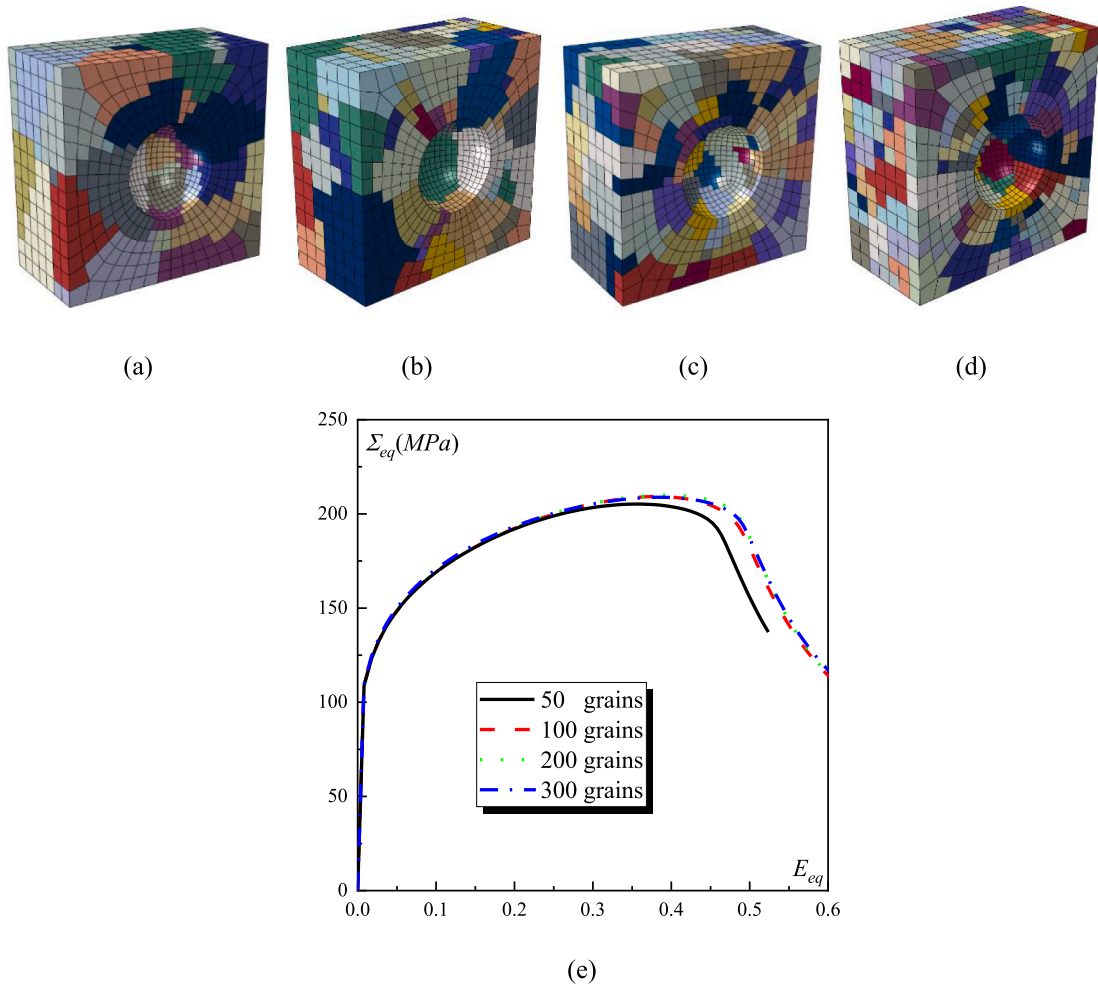


Fig. A1. Cross section view of voided unit cell containing: (a) 50, (b) 100, (c) 200, and (d) 300 grains. (e) Equivalent stress–strain responses corresponding to these four unit cells.

void coalescence is influenced by void shape, while void shape effect is maintained for a given crystallographic orientation. For polycrystalline aggregates, the texture effect is preserved for a given void shape and, conversely, the void shape effect is maintained for a given texture. On the other hand, the sensitivities of the two limit strains (E_{eq}^C and E_{eq}^B) and of their difference to the stress triaxiality are significantly dependent on the combined effects of crystallographic orientation and void shape. These findings are validated for both single crystals and polycrystalline aggregates.

Under proportional in-plane straining, only plastic strain localization in textured polycrystals containing different void shapes is predicted, since this plastic instability phenomenon is usually associated with forming limits of sheet metals. It is found that the initial void shape affects the level of forming limits for all the strain paths for a given initial texture. This enlarges the previous results presented in the literature, where the void shape was found to only affect the right-hand side of the FLDs when isotropic phenomenological models are adopted. This suggests that the use of crystal plasticity constitutive modeling allows accounting for the interaction between texture and void shape, which affects the macroscopic hardening behavior of the different UCs, thus resulting in perceptible influence on the left-hand side of the FLDs.

CRediT authorship contribution statement

J.C. Zhu: Conceptualization, Data curation, Writing – original draft, Visualization, Investigation, Validation, Methodology, Software. **M. Ben Bettaieb:** Conceptualization, Data curation, Writing – review & editing, Visualization, Validation. **F. Abed-Meraim:** Writing – review & editing, Validation, Formal analysis. **M.S. Huang:** Funding acquisition, Writing – review & editing, Validation. **Z. H. Li:** Writing – review & editing, Validation.

Declaration of Competing Interest

The authors declare that they have no known competing financial interests or personal relationships that could have appeared to influence the work reported in this paper.

Data availability

Data will be made available on request.

Acknowledgement

The authors would like to express their thanks for the financial support from NSFC (12072123, 12202153).

Appendix

Appendix A. Grain number sensitivity study

Regarding the representativeness of grain number, we have conducted a grain number sensitivity study. For this purpose, we compared the homogenized stress–strain responses of four spherically voided unit cells containing 50, 100, 200, 300 grains, as shown in Fig. A1.a, b, c, and d, respectively. A random texture is generated to define the crystallographic orientations of the grains constituting each of these four polycrystalline aggregates. Each unit cell is discretized by 5336 twenty-node finite elements (the same number of finite elements adopted in the simulations reported in the previous sections of the paper). As can be seen from Fig. A1.e, the grain number does not affect the stress–strain response as soon as more than 100 grains are used. In other words, unit cells containing 200 grains are indeed representative for the studied polycrystalline materials.

References

- [1] Tekoğlu C, Hutchinson JW, Pardoën T. On localization and void coalescence as a precursor to ductile fracture. *Philos Trans R Soc A Math Phys Eng Sci* 2015. <https://doi.org/10.1098/rsta.2014.0121>.
- [2] Zhu JC, Ben Bettaieb M, Abed-Meraim F. Investigation of the competition between void coalescence and macroscopic strain localization using the periodic homogenization multiscale scheme. *J Mech Phys Solids* 2020. <https://doi.org/10.1016/j.jmps.2020.104042>.
- [3] Gao B, Xiang Q, Guo T, Guo X, Tang S, Huang XX. In situ TEM investigation on void coalescence in metallic materials. *Mater Sci Eng A* 2018;734:260–8. <https://doi.org/10.1016/j.msea.2018.07.064>.
- [4] Guo Y, Burnett TL, McDonald SA, Daly M, Sherry AH, Withers PJ. 4D imaging of void nucleation, growth, and coalescence from large and small inclusions in steel under tensile deformation. *J Mater Sci Technol* 2022;123:168–76. <https://doi.org/10.1016/j.jmst.2022.01.024>.
- [5] Tekoğlu C, Koçhan B. Unit cell calculations under fully characterized stress states. *Int J Plast* 2022;156:103358. <https://doi.org/10.1016/j.ijplas.2022.103358>.
- [6] Liu ZG, Wong WH, Guo TF. Void behaviors from low to high triaxialities: Transition from void collapse to void coalescence. *Int J Plast* 2016;84:183–202. <https://doi.org/10.1016/j.ijplas.2016.05.008>.
- [7] Guo TF, Wong WH. Void-sheet analysis on macroscopic strain localization and void coalescence. *J Mech Phys Solids* 2018;118:172–203. <https://doi.org/10.1016/j.jmps.2018.05.002>.
- [8] Wong WH, Guo TF. On the energetics of tensile and shear void coalescences. *J Mech Phys Solids* 2015;82:259–86. <https://doi.org/10.1016/j.jmps.2015.05.013>.
- [9] Hosseini N, Nieto-Fuentes JC, Dakshinamurthy M, Rodríguez-Martínez JA, Vadillo G. The effect of material orientation on void growth. *Int J Plast* 2022;148. <https://doi.org/10.1016/j.ijplas.2021.103149>.
- [10] Tekoğlu C. Void coalescence in ductile solids containing two populations of voids. *Eng Fract Mech* 2015;147:418–30. <https://doi.org/10.1016/j.engfracmech.2015.07.004>.
- [11] Ha S, Kim K. Void growth and coalescence in f.c.c. single crystals. *Int J Mech Sci* 2010;52:863–73. <https://doi.org/10.1016/j.ijmecsci.2010.03.001>.
- [12] Yerra SK, Tekoğlu C, Scheyvaerts F, Delannay L, Van Houtte P, Pardoën T. Void growth and coalescence in single crystals. *Int J Solids Struct* 2010. <https://doi.org/10.1016/j.jisols.2009.12.019>.
- [13] Srivastava A, Needleman A. Void growth versus void collapse in a creeping single crystal. *J Mech Phys Solids* 2013;61:1169–84. <https://doi.org/10.1016/j.jmps.2013.01.006>.
- [14] Srivastava A, Needleman A. Effect of crystal orientation on porosity evolution in a creeping single crystal. *Mech Mater* 2015;90:10–29. <https://doi.org/10.1016/j.mechmat.2015.01.015>.
- [15] Guo HJ, Ling C, Busso EP, Zhong Z, Li DF. Crystal plasticity based investigation of micro-void evolution under multi-axial loading conditions. *Int J Plast* 2020. <https://doi.org/10.1016/j.ijplas.2020.102673>.
- [16] Ling C, Besson J, Forest S, Tanguy B, Latourte F, Bosso E. An elastoviscoplastic model for porous single crystals at finite strains and its assessment based on unit cell simulations. *Int J Plast* 2016;84:58–87. <https://doi.org/10.1016/j.ijplas.2016.05.001>.
- [17] Liu J, Huang M, Li Z, Zhao L, Zhu Y. Microvoid growth mechanism in FCC polycrystals and a statistical damage model. *Int J Plast* 2021;137:102888. <https://doi.org/10.1016/j.ijplas.2020.102888>.
- [18] Christodoulou PG, Dancette S, Lebensohn RA, Maire E, Beyerlein IJ. Role of crystallographic orientation on intragranular void growth in polycrystalline FCC materials. *Int J Plast* 2021;147. <https://doi.org/10.1016/j.ijplas.2021.103104>.
- [19] Luo T, Gao XS. On the prediction of ductile fracture by void coalescence and strain localization. *J Mech Phys Solids* 2018;113:82–104. <https://doi.org/10.1016/j.jmps.2018.02.002>.
- [20] Rice JR. The localization of plastic deformation. 14th Int. Congr. Theoretical Appl. Mech., 1976, p. 207–20. <https://doi.org/10.1.1.160.6740>.
- [21] Han X, Besson J, Forest S, Tanguy B, Bugat S. A yield function for single crystals containing voids. *Int J Solids Struct* 2013;50:2115–31. <https://doi.org/10.1016/j.jisols.2013.02.005>.
- [22] Shang X, Zhang H, Cui Z, Fu MW, Shao J. A multiscale investigation into the effect of grain size on void evolution and ductile fracture: Experiments and crystal plasticity modeling. *Int J Plast* 2020;125:133–49. <https://doi.org/10.1016/j.ijplas.2019.09.009>.

- [23] Koplik J, Needleman A. Void growth and coalescence in porous plastic solids. *Int J Solids Struct* 1988;24:835–53. [https://doi.org/10.1016/0020-7683\(88\)90051-0](https://doi.org/10.1016/0020-7683(88)90051-0).
- [24] Keralavarma SM, Hoelscher S, Benzerga AA. Void growth and coalescence in anisotropic plastic solids. *Int J Solids Struct* 2011;48:1696–710. <https://doi.org/10.1016/j.jeumechsol.2017.05.004>.
- [26] Keralavarma SM, Benzerga AA. A constitutive model for plastically anisotropic solids with non-spherical voids. *J Mech Phys Solids* 2010;58:874–901. <https://doi.org/10.1016/j.jmps.2010.03.007>.
- [27] Akpama HK, Ben Bettaieb M, Abed-Meraim F. Numerical integration of rate-independent BCC single crystal plasticity models: comparative study of two classes of numerical algorithms. *Int J Numer Methods Eng* 2016;108:363–422. <https://doi.org/10.1002/nme.5215>.
- [28] Ben Bettaieb M, Débordes O, Dogui A, Duchêne L, Keller C. On the numerical integration of rate independent single crystal behavior at large strain. *Int J Plast* 2012;32–33:184–217. <https://doi.org/10.1016/j.ijplas.2011.10.010>.
- [29] Yoshida K, Kuroda M. Comparison of bifurcation and imperfection analyses of localized necking in rate-independent polycrystalline sheets. *Int J Solids Struct* 2012;49:2073–84. <https://doi.org/10.1016/j.ijsolstr.2012.04.010>.
- [30] Raabe D, Roters F. Using texture components in crystal plasticity finite element simulations. *Int J Plast* 2004;20:339–61. [https://doi.org/10.1016/S0749-6419\(03\)00092-5](https://doi.org/10.1016/S0749-6419(03)00092-5).
- [31] Beausir B, Fundenberger J-J. Analysis Tools for Electron and X-ray diffraction, ATEX - software, www.atex-software.eu. Univ Lorraine - Metz 2017.
- [32] Lejeunes S, Bourgeois S. Une Toolbox Abaqus pour le calcul de propriétés effectives de milieux hétérogènes 10ème Colloq. Natl en Calc des Struct 2011:1–9.
- [33] Zhu JC, Ben Bettaieb M, Abed-Meraim F. Numerical investigation of necking in perforated sheets using the periodic homogenization approach. *Int J Mech Sci* 2020;166:105209. <https://doi.org/10.1016/j.ijmecsci.2019.105209>.
- [34] Miehe C. Computational micro-to-macro transitions for discretized micro-structures of heterogeneous materials at finite strains based on the minimization of averaged incremental energy. *Comput Methods Appl Mech Eng* 2003;192:559–91. [https://doi.org/10.1016/S0045-7825\(02\)00564-9](https://doi.org/10.1016/S0045-7825(02)00564-9).
- [35] Zhu JC, Ben BM, Abed-Meraim F. Comparative study of three techniques for the computation of the macroscopic tangent moduli by periodic homogenization scheme. *Eng Comput* 2022;38:1365–94. <https://doi.org/10.1007/s00366-020-01091-y>.
- [36] Ling C, Tanguy B, Besson J, Forest S, Latourte F. Void growth and coalescence in triaxial stress fields in irradiated FCC single crystals. *J Nucl Mater* 2017;492:157–70. <https://doi.org/10.1016/j.jnucmat.2017.04.013>.
- [37] Yoshida K, Ishizaka T, Kuroda M, Ikawa S. The effects of texture on formability of aluminum alloy sheets. *Acta Mater* 2007;55:4499–506. <https://doi.org/10.1016/j.actamat.2007.04.014>.
- [38] Akpama HK, Ben Bettaieb M, Abed-Meraim F. Localized necking predictions based on rate-independent self-consistent polycrystal plasticity: Bifurcation analysis versus imperfection approach. *Int J Plast* 2017;91:205–37. <https://doi.org/10.1016/j.ijplas.2017.02.001>.
- [39] Tenreiro Vieira RR, De Bortoli D, Vieira De Carvalho M, Andrade Pires FM. The role of elastic anisotropy on the macroscopic constitutive response and yield onset of cubic oligo- And polycrystals. *Int J Plast* 2019;121:153–200. <https://doi.org/10.1016/j.ijplas.2019.06.007>.